

Gravitational radiation from nonaxisymmetric spherical Couette flow in a neutron star

C. Peralta,^{1,2} A. Melatos,¹ M. Giacobello³ and A. Ooi³

cperalta@physics.unimelb.edu.au

ABSTRACT

The gravitational wave signal generated by global, nonaxisymmetric shear flows in a neutron star is calculated numerically by integrating the incompressible Navier-Stokes equation in a spherical, differentially rotating shell. At Reynolds numbers $Re > 3 \times 10^3$, the laminar Stokes flow is unstable and helical, oscillating Taylor-Görtler vortices develop. The gravitational wave strain generated by the resulting kinetic-energy fluctuations is computed in both $+$ and \times polarizations as a function of time. It is found that the signal-to-noise ratio for a coherent, 10^8 -s integration with LIGO II scales as $6.5 (\Omega = 10^4 \text{ rad s}^{-1})^{7/2}$ for a star at 1 kpc with angular velocity Ω . This should be regarded as a lower limit: it excludes pressure fluctuations, herringbone flows, Stuart vortices, and fully developed turbulence (for $Re > 10^6$).

Subject headings: gravitational waves | hydrodynamics | stars: neutron | stars: rotation

1. Introduction

Gravitational radiation from linear, global, fluid oscillations in neutron stars has been studied extensively, e.g. radiation-reaction-driven modes (Andersson 1998; Levin & Ushomirsky 2001), and two-stream superfluid oscillations with entrainment (Andersson 2003; Prix et al. 2004). However, gravitational radiation is also emitted by nonlinear, global, fluid oscillations. Specifically, it is well known that a viscous Navier-Stokes fluid inside a spherical, differentially rotating shell | spherical Couette flow (SCF) | undergoes sudden transitions

¹School of Physics, University of Melbourne, Parkville, VIC 3010, Australia

²Departamento de Física, Escuela de Ciencias, Universidad de Oriente, Cumana, Venezuela

³Department of Mechanical Engineering, University of Melbourne, Parkville, VIC 3010, Australia

between states with different vortex topologies, which are generally nonaxisymmetric, due to shear instabilities (Marcus & Tuckerman 1987a,b; Junk & Egbers 2000). Recent simulations of superfluid SCF, based on the Hall-Vinen-Bekarevich-Khalatnikov (HVBK) theory of a 1S_0 neutron superfluid, confirm that such transitions to nonaxisymmetric flows also occur in neutron stars (Peralta et al. 2005, 2006).

In this Letter, we compute the gravitational wave signal generated by nonaxisymmetric flows in young, rapidly rotating neutron stars. There are at least two astrophysical scenarios in which these develop. First, if the crust and core of the star are loosely coupled, as indicated by observations of pulsar glitches (Shemar & Lyne 1996; Lyne et al. 2000), differential rotation builds up as the crust spins down electromagnetically, until the core undergoes a transition to the Taylor-Görtler vortex state, a helical, oscillating flow that is one of the last stages in the laminar-turbulent transition in SCF as the Reynolds number increases (Nakabayashi 1983; Nakabayashi & Tsuchida 1988). Second, if the crust precesses, while the core does not, the rotation axes of the crust and core misalign, inducing a rich variety of flow patterns and instabilities, like time-dependent shear waves, leading to fully developed turbulence (Wilde & Vanyo 1995). We treat the former scenario here and postpone the latter to a separate paper.

In §2, an SCF model of a differentially rotating neutron star is proposed. In §3, we explore the transitional dynamics and topology of the flow. In §4, we calculate the gravitational wave signal and its frequency spectrum.

2. Global SCF model and numerical method

We consider an idealized, two-component model of a neutron star, in which a solid crust is loosely coupled to a differentially rotating fluid core. Specifically, we consider the motion of a neutron fluid within a spherical, differentially rotating shell in the outer core of the star, where the density lies in the range $0.6 < \rho_c < 1.5$, $\rho_c = 2.6 \times 10^4 \text{ g cm}^{-3}$ (Sedrakian & Sedrakian 1995). The inner (radius R_1) and outer (radius R_2) boundaries rotate at angular frequencies Ω_1 and Ω_2 , respectively, about the z axis. As the star is strongly stratified, the shell is thin, with $R_2 - R_1 \ll R_1$ (Abney & Epstein 1996; Levin & D'Angelis 2004). The rotational shear is sustained by the vacuum-dipole spin-down torque, violent events at birth (Dimmelmeier et al. 2002; Ott et al. 2004), accretion in a binary (Fujimoto 1993), neutron star mergers (Shibata & Uryu 2000), or internal oscillations like r-modes (Rezzolla et al. 2000; Levin & Ushomirsky 2001).

We describe the fluid by the isothermal Navier-Stokes equation, which, in the inertial

frame of an external observer, takes the form

$$\frac{\partial \mathbf{v}}{\partial t} + (\mathbf{v} \cdot \nabla) \mathbf{v} = -\frac{\nabla p}{\rho} + \nabla^2 \mathbf{v} + \nabla \Phi \quad (1)$$

in the incompressible limit $\nabla \cdot \mathbf{v} = 0$, where \mathbf{v} is the fluid velocity, ν is the kinematic viscosity, ρ is the density, p is the pressure, and Φ is the Newtonian gravitational potential. Henceforth, ν is absorbed into p by replacing ∇p with ∇p , such that pressure balances gravity in the stationary equilibrium ($\mathbf{v} = 0$) and there are no gravitational forces driving the flow in the incompressible limit when the stationary equilibrium is perturbed. The Reynolds number and dimensionless gap width are defined by $Re = \frac{v}{\nu} R_1^2 = \frac{v}{\nu} R_1^2$ and $\delta = (R_2 - R_1)/R_1$; the rotational shear is $\Omega = \Omega_2 - \Omega_1$. Equation (1) is solved subject to no-slip boundary conditions.

Superfluidity plays a central role in the thermal (Yakovlev et al. 1999) and hydrodynamic (Alpar 1978; Reisenegger 1993; Peralta et al. 2005) behavior of neutron star interiors. However, we assume a viscous fluid here. Counterintuitively, this is a good approximation because $Re \sim 10^{11}$ is very high (Mastrano & Melatos 2005). It is known from terrestrial experiments on superfluid ^4He that, at high Re , quantized vortices tend to lock the superfluid to turbulent eddies in the normal fluid by mutual friction (Barenghi et al. 1997), so that the superfluid resembles classical Navier-Stokes turbulence. Moreover, in HVBK simulations of SCF, it is observed that the global circulation pattern of the superfluid does not differ much from a Navier-Stokes fluid at $Re > 250$ (Henderson & Barenghi 2004; Peralta et al. 2005). Finally, a viscous interior is expected in newly born neutron stars, which are hotter than the superfluidity transition temperature (Andersson et al. 1999).

By assuming a viscous fluid, we omit from (1) the coupling between quantized vortices and the normal fluid (Hall & Vinen 1956), entrainment of superfluid neutrons by protons (Comer 2002), and pinning of quantized vortices in the inner crust, at radius R_1 [Baym et al. (1992); cf. Jones (1998)]. We also neglect vortex pinning in the outer core for simplicity, even though evidence exists that it may be important when magnetic fields are included. Specifically, three-fluid models of post-glitch relaxation based on the core dynamics favor vortex pinning at the phase separation boundary of the core (Sedrakian & Sedrakian 1995), e.g. due to the interaction between vortex clusters and the Meissner supercurrent set up by the crustal magnetic field at the phase boundary (Sedrakian & Cordes 1999). Other models analyze interpinning of proton and neutron vortices in the core (Ruderman 1991) and its effect on precession (Link 2003). In the context of the hydrodynamic model in this paper, pinning effectively increases the viscosity of the core, reducing Re .

We use a pseudospectral collocation method to solve equation (1) (Bagchi & Balachandrar 2002; Giacobello 2005). The equations are spatially discretized in spherical polar coord-

ordinates $(r; \theta; \phi)$, using restricted Fourier expansions in θ and ϕ and a Chebyshev expansion in r . The solution is advanced using a two-step fractional-step method, which is accurate to second order in the time-step (Canuto et al. 1988). We limit ourselves to narrow gaps 0.1 , which are computationally less expensive and for which more experimental studies are available for comparison (Yavorskaya et al. 1977; Nakabayashi 1983). Recently, we performed the first stable simulations of superfluid SCF using this method (Peralta et al. 2005).

3. Nonaxisymmetric spherical Couette flow

The bifurcations and instabilities leading to transitions between SCF states are controlled by three parameters: Ω , Re , and Γ . Additionally, the history of the flow influences its post-instability evolution and the final transition to turbulence (Wulf et al. 1999; Junk & Egbers 2000). For example, in experiments on Taylor-Görtler vortices (TGV), the final state depends on $d_1 = dt$, i.e. on the time to reach the critical Re relative to the viscous diffusion time (Nakabayashi & Tsuchida 1995). In general, four SCF states can be distinguished: (i) a laminar basic flow, (ii) a toroidal or helical Taylor-Görtler flow, (iii) a transitional flow with nonaxisymmetric, oscillating TGV, and (iv) fully developed turbulence (Yavorskaya et al. 1975; Nakabayashi 1983). In a neutron star, where $Re \sim 10^{11}$, the state is probably turbulent. However, we are restricted by our computational resources to simulate regimes (i) and (ii), with $1 \leq Re \leq 3 \times 10^4$.

3.1. TGV transition: initial conditions

Experimentally, for $\Gamma = 0.06$, TGV are obtained by quasistatically increasing Ω from zero to give $Re \sim 3300$ (Nakabayashi & Tsuchida 2005). This procedure can be painfully slow, because a steady state must be reached at each intermediate step. Numerically, we circumvent it by following Li (2004) and introducing a nonaxisymmetric perturbation with azimuthal wave number m_a of the form

$$v_r = \frac{4 \Omega_1 (r - R_1)(r - R_2)}{2R_1^2} \cos(\theta; \phi); \tag{2}$$

$$v_\theta = \frac{1}{2} \sin \frac{(r - R_1)(r - R_2)}{(R_2 - R_1)^2} \sin(\theta; \phi); \tag{3}$$

with $\Omega = [\Omega_0 + \Omega_1 (2 - \frac{r}{R_2})] \Omega_0 \sin(m_a \theta)$. This is done as follows. Before introducing the perturbation, a steady state for $Re = 2667$ is obtained (just below the critical Re

where TGV emerge experimentally). Then, the Reynolds number is raised instantaneously to $Re = 3300$, and we continue by adding (2) and (3), with amplitude $\delta = 10^{-6} R_1$, to the numerical solution at each time-step until a viscous diffusion time $t_d = (R_2 - R_1)^2 = \tau$ elapses. We then stop adding the perturbation and the flow is left to evolve according to (1), until a final steady state is reached. More than one perturbation can lead to the same final state; some authors add Gaussian noise (Zikanov 1996), although this affords less control over the wavenumber and the number of vortices excited.

The perturbation excites TGV by shedding vorticity from the inner sphere (Li 2004). Perturbations with $2 \leq m_a \leq 5$ are explored, supplementing experiments with $m_a = 3$ (Nakabayashi 1983). For numerical simplicity, we limit ourselves to the case where only the inner sphere rotates. TGV with both spheres rotating are equally possible and have been observed experimentally; they exhibit additional twisting (and increased nonaxisymmetry) in the helical vortices (Nakabayashi & Tsuchida 2005), so the gravitational wave strain we compute in x4 is a lower limit.

3.2. Flow topology

Figure 1a shows a kinetic-energy-density isosurface ($0.11 R_1^5 \tau^{-2}$) for the fully developed TGV state $m_a = 3$, $\tau = 0.06$, $Re = 3300$. Its nonaxisymmetry is apparent in the striated equatorial bands, whose inclination with respect to the equator varies with longitude from zero to ≈ 3 deg (Nakabayashi 1983).

A popular way to classify complex, three-dimensional flows is to construct scalar invariants from $A_{ij} = \partial v_i / \partial x_j$ (Chong et al. 1990; Jeong & Hussain 1995). Specifically, the discriminant $D_A = Q_A^3 + 27R_A^2 = 4$, with $R_A = \det(A_{ij})$ and $Q_A = (A_{ii}^2 - A_{ij}A_{ji})/2$, distinguishes between regions which are focal ($D_A > 0$) and strain-dominated ($D_A < 0$). Figure 1b plots the $D_A = 10^{-3} \tau^{-6}$ isosurface in color: yellow regions are stable focus/stretching,⁴ blue regions are unstable focus/contracting. The filaments coincide with the TGV. One circumferential vortex and $m_a = 3$ helical vortices lie in each hemisphere. We also plot the isosurface $D_A = -10^{-3} \tau^{-6}$: red and green regions have stable node/saddle/saddle and unstable node/saddle/saddle topologies respectively (Chong et al. 1990). The helical vortices span ≈ 40 deg of latitude and travel in the \hat{z} direction, with phase speed $\approx 0.48 R_1$.

The TGV state is oscillatory, which is important for the gravitational wave spectrum.

⁴Trajectories are repelled away from a fixed point along a real eigenvector of A_{ij} (stretch) and describe an inward spiral when projected onto the plane normal to the eigenvector (stable focus).

Its periodicity is evident in Figure 1c, where v at an equatorial point is plotted versus time for $2 \leq m_a \leq 5$. For $m_a = 3$, v oscillates with period $4:4 \text{ s}^{-1}$, the time for successive helical vortices to pass by a stationary observer, in accord with experiments (Nakabayashi 1983). Instantaneous stream lines are drawn in three meridional planes in Figure 1d, highlighting the nonaxisymmetry. One obtains a similar TGV state for $\beta = 0:14, = 0:18$ (Sha & Nakabayashi 2001; Li 2004).

4. Gravitational wave signal

The metric perturbation $h_{ij}^{TT} = (4G/rc^4) \int d^3x T_{ij}$ in the transverse-traceless gauge can be calculated using Einstein's quadrupole formula (Misner et al. 1973)

$$h_{ij}^{TT} = \frac{2G}{rc^6} \frac{\partial^2}{\partial t^2} \int d^3x \left[\frac{1}{2} \ddot{x}_i \ddot{x}_j + \frac{1}{3} \ddot{x}_i \ddot{x}_j \right]; \quad (4)$$

where the integral is over the source volume, r is the distance to the source, and $T_{ij} = \rho v_i v_j + p \delta_{ij}$ is the stress-energy of a Newtonian fluid. Note that we approximate $T_{00} = \rho c^2 (1 + \frac{1}{2} \dot{x}_i \dot{x}_i)$ in (4), and we omit a thermal-energy contribution ρp (by Bernoulli's theorem), which we cannot calculate with our incompressible solver. Far from the source, we write $h_{ij}^{TT} = h_+ e_{ij}^+ + h_\times e_{ij}^\times$, with the polarizations defined by $e_{yy}^+ = e_{zz}^\times = e_{yz} = e_{zy} = 1$ for an observer on the x axis.

In Figure 2a, we plot the h_+ and h_\times polarizations versus time, as seen by an observer on the x axis, for $2 \leq m_a \leq 5$ (the signal is 3 times weaker on the z axis, where the north-south asymmetry is not seen in projection). The amplitude is greatest for $m_a = 5$ but depends weakly on m_a . Importantly, h_+ and h_\times are $\pi/2$ out of phase for all m_a , and we find $\dot{h}_+ \dot{h}_\times$ for even m_a . These two signatures offer a promising target for future observations. The period ($0:8 \text{ s}^{-1}$) is similar for $3 \leq m_a \leq 5$, where a maximum of three helical vortices are excited (Li 2004) (we find that the torque at R_2 oscillates with the same period). This too is good for detection, because several modes are likely to be excited in a real star. The period arises because the isosurface in Figure 1a forms a pattern with six-fold symmetry when projected onto the y - z plane, with fundamental period $4:4 \text{ s}^{-1}$.

In Figure 2b, we present the frequency spectra of the h_+ and h_\times polarizations. The two peaks, at $f = 1:2 \text{ s}^{-1}$ and $2:4 \text{ s}^{-1}$, have full-width-half-maxima of $\approx 300 \text{ Hz}$. This is caused by the subharmonics evident in Figure 1c, which arise because the northern and southern helical vortices start at unequal and variable longitudes. In addition, the peaks for even and odd m_a are displaced by $\approx 500 \text{ Hz}$, and the primary peak for $m_a = 4$ is split. These two spectral signatures are a promising target for future observations. The even-odd displacement may

arise because the phase speeds of the vortex patterns for $m_a = 2, 3$ differ by $\sim 0.01 \Omega R_1$ (Li 2004). For large f , we find $h_+ \propto (f) / f^{3/2}$.

The squared signal-to-noise ratio can be calculated from $(S/N)^2 = 4 \int_0^{R_1} df \dot{h}(f) \dot{h}^* = S_h(f)$ (Creighton 2003), where we take $S_h(f) = 10^{-50} (f/0.6 \text{ kHz})^2 (0.2 \leq f \leq 3 \text{ kHz})$ for a 10-s integration with LIGO II, if the frequency and phase of the signal are known in advance (Brady et al. 1998). For a star with $\Omega = 600 \text{ Hz}$, at $r = 1 \text{ kpc}$, we find $S/N = 0.21$ ($m_a = 2$), 0.12 ($m_a = 3$), 0.023 ($m_a = 4$), and 0.22 ($m_a = 5$), although there will be some leakage of signal when the coherent integration is performed, because the spectrum is not monochromatic. For $m_a \leq 5$, S/N increases (decreases) as m_a odd (even) increases. We also find $S/N \propto \Omega^{7/2}$, which implies that the fastest millisecond pulsars ($\Omega = 1 \text{ kHz}$) and newly born pulsars with $\Omega = 0.1$ are most likely to be detected. The flow states leading to turbulence at $Re > 10^6$, e.g. shear waves, Stuart vortices, and "herringbone" waves (Nakabayashi & Tsuchida 1988), make contributions of similar order to the TGV signal in Figure 2.

The Reynolds number in the outer core of a neutron star, $Re = 10^{10} (\rho = 10^{15} \text{ g cm}^{-3})^{-1/2} (T = 10^8 \text{ K})^2 (\Omega = 10^4 \text{ rad s}^{-1})$ (Mastrano & Melatos 2005), where T is the temperature, typically exceeds the maximum Re in our simulations (due to computational capacity). For $Re > 10^6$, the flow is turbulent and therefore axisymmetric when time-averaged but not instantaneously. In Kolmogorov turbulence, the characteristic flow speed in an eddy of wavenumber k scales as $k^{-1/3}$, the turbulent kinetic energy scales as $k^{-5/3}$, and the turnover time scales as $k^{-2/3}$. From equation (4), the rms wave strain scales as $k^{-3/2} \int dk k^{-1/3}$ after averaging over Gaussian fluctuations, and is dominated by the largest eddies (where most of the kinetic energy also resides). We therefore conclude that, even for $Re > 10^6$, the largest eddies, which resemble organized structures like TGV, dominate h_+ and h_- , not the isotropic small eddies, but the signal is noisier. Hence, counterintuitively, we predict that hotter neutron stars (with lower Re) have narrower gravitational wave spectra than cooler neutron stars, ceteris paribus.

We ignore compressibility when computing T_{00} ($p = 0$) and solving (1) numerically by pressure projection. Yet, realistically, neutron stars are strongly stratified (Abney & Epstein 1996), confining the meridional flow in Figure 1d into narrow layers near $r = R_1, R_2$. Stratification can be implemented crudely by using a low-pass spectral filter to artificially suppress v_r (Don 1994; Peralta et al. 2006). We postpone this to future work.

We acknowledge the computer time supplied by the Australian Partnership for Advanced Computation (APAC). We thank Prof. Li Yuan, from the Chinese Academy of Sciences, for very helpful discussions.

REFERENCES

- Abney, M ., & Epstein, R . I. 1996, *J. Fluid Mech.*, 312, 327
- Alpar, M . A . 1978, *J. Low Temp. Phys.*, 31, 803
- Andersson, N . 1998, *ApJ*, 502, 708
- | . 2003, *Classical Quant. Grav.*, 20, 105
- Andersson, N ., Kokkotas, K ., & Schutz, B . F . 1999, *ApJ*, 510, 846
- Bagchi, B ., & Balachandar, S. 2002, *J. Fluid. Mech.*, 466, 365
- Barenghi, C . F ., Samuels, D . C ., Bauer, G . H ., & Donnelly, R . J. 1997, *Phys. Fluids*, 9, 2631
- Baym , G ., Epstein, R ., & Link, B . 1992, *Physica B* , 178, 1
- Brady, P . R ., Creighton, T ., Cutler, C ., & Schutz, B . F . 1998, *Phys. Rev. D* , 57, 2101
- Canuto, C ., Hussaini, M ., Quarteroni, A ., & Zang, T . 1988, *Spectral Methods in Fluid Dynamics* (Springer-Verlag)
- Chong, M . S ., Perry, A . E ., & Cantwell, B . J. 1990, *Phys. Fluids*, 2, 765
- Comer, G . L. 2002, *Found. Phys.*, 32, 1903
- Creighton, T . 2003, *Classical Quant. Grav.*, 20, 853
- Dinmelmeyer, H ., Font, J. A ., & Muller, E . 2002, *A & A* , 393, 523
- Don, W . S. 1994, *J. Comput. Phys.*, 110, 103
- Fujimoto, M . Y . 1993, *ApJ*, 419, 768
- Giacobello, M . 2005, PhD thesis, University of Melbourne
- Hall, H . E ., & Vinen, W . F . 1956, *Proc. R . Soc. Lond.*, A 238, 204
- Henderson, K . L ., & Barenghi, C . F . 2004, *Theor. Comp. Fluid Dyn.*, 18, 183
- Jeong, J ., & Hussain, F . 1995, *J. Fluid Mech.*, 285, 69
- Jones, P . B . 1998, *MNRAS*, 296, 217
- Junk, M ., & Egbers, C . 2000, *LNP Vol. 549: Physics of Rotating Fluids*, 549, 215

- Levin, Y., & D'Angelis, C. 2004, *ApJ*, 613, 1157
- Levin, Y., & Ushomirsky, G. 2001, *MNRAS*, 324, 917
- Li, Y. 2004, *Sci. China Ser. A*, 47, 81
- Link, B. 2003, *Phys. Rev. Lett.*, 91, 101101
- Lyne, A. G., Shemar, S. L., & Smith, F. G. 2000, *MNRAS*, 315, 534
- Marcus, P., & Tuckerman, L. 1987a, *J. Fluid Mech.*, 185, 1
|. 1987b, *J. Fluid Mech.*, 185, 31
- Mastrano, A., & Melatos, A. 2005, *MNRAS*, 361, 927
- Misner, C. W., Thorne, K. S., & Wheeler, J. A. 1973, *Gravitation* (San Francisco: W. H. Freeman and Co., 1973)
- Nakabayashi, K. 1983, *J. Fluid Mech.*, 132, 209
- Nakabayashi, K., & Tsuchida, Y. 1988, *J. Fluid Mech.*, 194, 101
|. 1995, *J. Fluid Mech.*, 295, 43
|. 2005, *Phys. Fluids*, 17, 4110
- Ott, C. D., Burrows, A., Livne, E., & Walder, R. 2004, *ApJ*, 600, 834
- Peralta, C., Melatos, A., Giacobello, M., & Ooi, A. 2005, *ApJ*, 635, 1224
|. 2006, Submitted to *ApJ*
- Prix, R., Comer, G. L., & Andersson, N. 2004, *MNRAS*, 348, 625
- Reisenegger, A. 1993, *J. Low Temp. Phys.*, 92, 77
- Rezzolla, L., Lamb, F. K., & Shapiro, S. L. 2000, *ApJ*, 531, L139
- Ruderman, M. 1991, *ApJ*, 382, 587
- Sedrakian, A., & Cordes, J. M. 1999, *MNRAS*, 307, 365
- Sedrakian, A. D., & Sedrakian, D. M. 1995, *ApJ*, 447, 305
- Sha, W., & Nakabayashi, K. 2001, *J. Fluid Mech.*, 431, 323

Shenar, S. L., & Lyne, A. G. 1996, *MNRAS*, 282, 677

Shibata, M., & Uryu, K. o. 2000, *Phys. Rev. D*, 61, 064001

Wilde, P. D., & Vanyo, J. P. 1995, *Phys. Earth Planet. In.*, 91, 31

Wulf, P., Egbers, C., & Rath, H. J. 1999, *Phys. Fluids*, 11, 1359

Yakovlev, D. G., Leven sh, K. P., & Shibanov, Y. A. 1999, *Usp. Fiz. Nauk*, 42, 737

Yavorskaya, I. M., Belayev, Y. N., & Monakhov, A. A. 1975, *Sov. Phys. Dokl.*, 20 (4), 209

| . 1977, *Sov. Phys. Dokl.*, 22 (12), 717

Zikanov, O. Y. 1996, *J. Fluid Mech.*, 310, 293

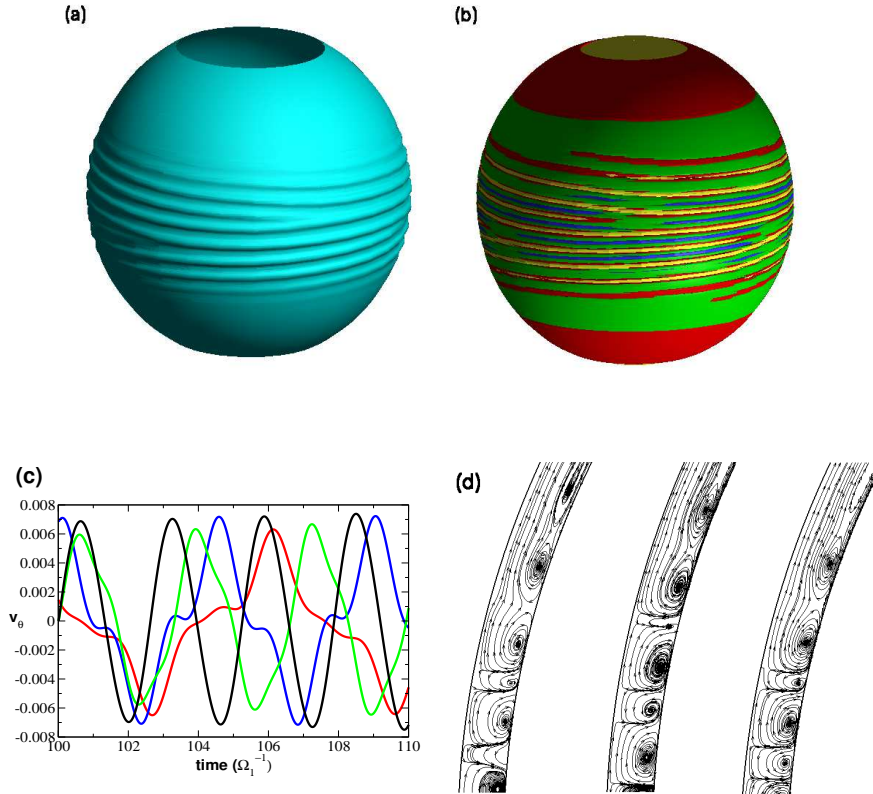


Fig. 1. | Taylor-Görtler vortices for $m_a = 3$, $\epsilon = 0.06$, at $t = 100 \Omega_1^{-1}$. (a) Isosurface of kinetic energy: $|\mathbf{v}|^2 = 0.11 R_1^5 \Omega_1^2$. (b) Isosurfaces of velocity-gradient discriminant: $D_A = 10^3 \Omega_1^6$, stable focus/stretching (yellow) and unstable focus/contracting (blue); $D_A = 10^3 \Omega_1^6$, stable node/saddle/saddle (red) and unstable node/saddle/saddle (green). (c) Time history of v_θ at $r = 1.06$, $\theta = 2$, $\phi = 0$ for $m_a = 2$ (red), 3 (blue), 4 (green), and 5 (black). (d) Stream lines obtained by integrating the in-plane components of v in the planes $\theta = 0$ (left), $\theta = 2$ (middle), and $\theta = 2.9$ (right).

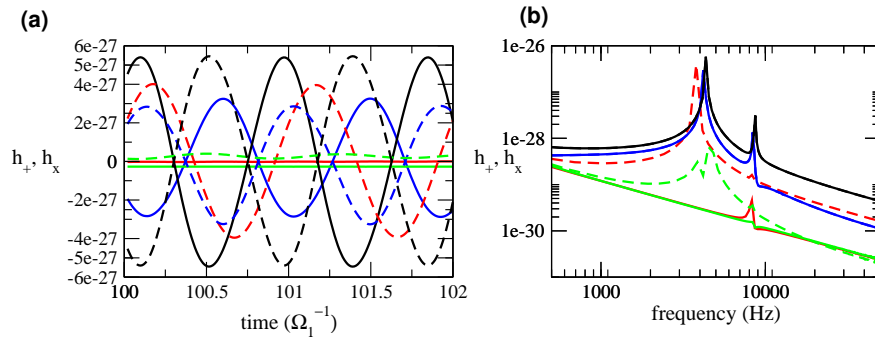


Fig. 2. | Gravitational waves from Taylor-G order vortices in a neutron star with $\ell_1=2$, $m_1=600$ Hz and $r = 1$ kpc. (a) Signal h_+ , h_x vs time, and (b) frequency spectrum h_+ , h_x vs frequency, for $m_a = 2$ (red), 3 (blue), 4 (green), and 5 (black). Solid and dashed curves correspond to the $+$ and x polarizations respectively, as measured by an observer on the x axis.